Exact density matrix of the Gutzwiller wave function as the ground state of the inverse-square supersymmetric t-J model. II. Minority spin component

Exact density matrix of the Gutzwiller wave function as the ground state of the inverse-square supersymmetric *t-J* model. II. Minority spin component

Onuttom Narayan
Department of Physics, University of California, Santa Cruz, California 95064, USA

Yoshio Kuramoto
Department of Physics, Tohoku University, Sendai 980-8578, Japan

Mitsuhiro Arikawa
Institute of Physics, University of Tsukuba, Tsukuba 305-8571 Japan

(Received 24 August 2007; published 14 January 2008)

The density matrix, i.e., the Fourier transform of the momentum distribution, is obtained analytically for all values of the magnetization of the Gutzwiller wave function in one dimension with the exclusion of double occupancy per site. The present result complements the previous analytic derivation of the density matrix for the majority spin. The derivation makes use of a determinantal form of the squared wave function, and multiple integrals over particle coordinates are performed with the help of a diagrammatic representation. In the thermodynamic limit, the density matrix at distance x is completely characterized by quantities $v_c x$ and $v_s x$, where v_s and v_c are spin and charge velocities in the supersymmetric *t-J* model for which the Gutzwiller wave function gives the exact ground state. The present result then gives the exact density matrix of the *t-J* model for all densities and all magnetization at zero temperature. Discontinuity, slope, and curvature singularities in the momentum distribution are identified. The momentum distribution obtained by numerical Fourier transform is in excellent agreement with existing results.

DOI: 10.1103/PhysRevB.77.045114 PACS number(s): 71.10.−w, 71.27.+a

I. INTRODUCTION

The Gutzwiller wave function is the simplest many-particle wave function capable of capturing both itinerant and localized characters of strongly correlated electrons.[1] For a long time, it has been considered as a variational wave function for standard models such as the Hubbard model and the *t-J* model.[2,3] It is now known that the Gutzwiller wave function without double occupancy for each site constitutes the exact ground state for the supersymmetric *t-J* model in one dimension, for which both the exchange and transfer terms in the Hamiltonian decay as an inverse square of the distance.[4] Given this context, it is highly meaningful to derive exact properties for the Gutzwiller wave function without double occupation per site. Various quantities have been studied exactly such as the spin and charge correlation functions and the momentum distribution, which is the Fourier transform of the density matrix. Although the correlation functions have been obtained in a simple closed form,[5,6] most results for the momentum distribution still involve a final integration or a summation over an infinite series.[7–9]

For a case with finite magnetization, Kollar and Vollhardt[8] extended the method of Ref. 7 and obtained the infinite series expansion of the momentum distribution. The expansion is valid for general dimensions and a general degree of restricting the double occupation. In one dimension, they could sum up the series into a form involving a single integral over elliptic functions. The resultant mathematical form is very complicated, and it is difficult to obtain any insight from the final formula in Ref. 8.

On the other hand, a completely different approach has been taken by Arikawa *et al.*[9,10] Namely, the exact Green function is integrated over the energy to give the momentum distribution. The result has been obtained only for the singlet ground state and still involves integrals. However, the structure of the integral makes it clear how the elementary excitations of spin and charge determine the momentum distribution.

In a previous paper,[11] hereafter referred to as Paper I, we adopted another approach and derived the exact density matrix of the Gutzwiller wave function in a closed form. Our results in Paper I, however, have been restricted to the majority spin component. In this paper, we derive the minority spin component, completing the analytic derivation for all magnetizations and all densities. In the singlet ground state without magnetization, the limit from the minority spin agrees with that from the majority spin.

Our strategy in Paper I and in this paper is to approach the real space instead of the momentum space. In the real space, all singularities in the momentum distribution appear in the asymptotic behavior of the density matrix. Hence, we can avoid dividing the momentum space into different regions separated by characteristic momenta. This paper gives the explicit form of the density matrix with the use of Bessel functions. The form obtained allows interpretation in terms of elementary excitations of spin and charge. It is remarkable that different spin and charge velocities combine in such a way as to reproduce the asymptotic behavior expected from the combination of the Fermi momenta of up and down spins.

II. GUTZWILLER WAVE FUNCTION IN JASTROW FORM

We work with the particular representation of the Gutzwiller wave function with the exclusion of double occu-

pancy at each site. We choose as the reference state the fully polarized state $|F\rangle$, where each site is occupied by an up spin.[12] Then, a down spin at site j is created by operating with $S_j^- = S_j^x - iS_j^y$ on $|F\rangle$, and a hole by $h_j^\dagger = c_{j\downarrow} S_j^-$. Note that h_j does not obey the ordinary anticommutation rule of fermions. We can represent any state in terms of the wave function $\Psi(\{x^s\},\{x^h\})$ as[12]

$$|\Psi\rangle = \sum_{\{x^s\},\{x^h\}} \Psi(\{x^s\},\{x^h\}) \prod_{i\in\{x^s\}} S_i^- \prod_{j\in\{x^h\}} h_j^\dagger |F\rangle, \tag{1}$$

where the set of coordinates $\{x^s\}$ specifies the positions of M magnons, and $\{x^h\}$ specifies those of Q holes. We call this scheme the magnon-hole representation. The hard-core constraint is satisfied by the property $(S_j^-)^2 = (h_j^\dagger)^2 = S_j^- h_j^\dagger = 0$. By definition, $\Psi(\{x^s\},\{x^h\})$ is symmetric against the interchange of down-spin coordinates and antisymmetric against hole coordinates. This is related to the commutation rule $S_i^- S_j^- = S_j^- S_i^-$ and the anticommutation rule $h_i^\dagger h_j^\dagger = -h_j^\dagger h_i^\dagger$ for $i \neq j$. Furthermore, we have the relation $S_i^- h_j^\dagger = h_j^\dagger S_i^-$.

The Gutzwiller wave function is represented in the magnon-hole representation by

$$\Psi_G(\{x^s\},\{x^h\}) = \prod_{j=1}^{M+Q} \exp(i\pi x_j) \prod_{i<j} D(x_i^s - x_j^s)^2 \times \prod_{l<m} D(x_l^h - x_m^h) \prod_{i,l} D(x_i^h - x_l^s), \tag{2}$$

where $D(i-j) = (L/\pi)\sin[\pi(i-j)/L]$ and x_j denotes both hole $(j=1,\ldots,Q)$ and magnon $(j=Q+1,\ldots,M+Q)$ coordinates. This form is valid for non-negative magnetization, i.e., $2M+Q \leqslant L$. We have omitted a normalization factor here. Here, we have assumed the simplest case of L and M even, and Q odd,[13] for which the ground state is nondegenerate. In the thermodynamic limit, the result does not depend on the choice of even or odd numbers of particles. The momentum associated with $\Psi_G(\{x^s\},\{x^h\})$ is π because we have taken $M+Q$ odd. However, the reference state $|F\rangle$ itself has momentum π since the occupied set of momentum includes one of the Brillouin zone boundary π, which does not cancel with the rest of the occupied momentum. Thus, the Gutzwiller state $|\Psi_G\rangle$ has zero momentum because of the cancellation of π in $|F\rangle$ and $\Psi_G(\{x^s\},\{x^h\})$.

It is convenient to introduce the complex coordinate $z_j = \exp(2\pi i x_j/L)$ for both magnons and holes using the identity

$$2i \sin[\pi(x_i - x_j)/L] = (z_i - z_j)/\sqrt{z_i z_j}. \tag{3}$$

Then, the Gutzwiller wave function is given as a polynomial of these complex coordinates, apart from the factor for the Galilean boost. We work with the form

$$\Psi_G(\{z\}) = \Psi_{m+h}(\{z\}) \Psi_m(\{z\}), \tag{4}$$

where the factors in the right-hand side are given by

$$\Psi_{m+h}(\{z\}) = i^{-(M+Q)(M+Q-1)/2} \prod_{i=1}^{Q+M} z_i^{L/2-(Q+M-1)/2} \prod_{i<j} (z_i - z_j) \tag{5}$$

and

$$\Psi_m(\{z\}) = i^{-M(M-1)/2} \prod_{i=Q+1}^{Q+M} z_i^{-(M-1)/2} \prod_{Q<i<j\leqslant Q+M} (z_i - z_j), \tag{6}$$

where we have dropped factors of $L/(2\pi)$ from each $(z_i - z_j)$, as compared with Eq. (2).

The Gutzwiller wave function given by Eq. (2) turns out to give the exact ground state of the t-J model with a special condition for the transfer and the exchange interaction.[4] The t-J model in general is given by

$$\mathcal{H}_{tJ} = \sum_{i<j} \mathcal{P}\left[-t_{ij} \sum_{\sigma=\uparrow,\downarrow} (c_{i\sigma}^\dagger c_{j\sigma} + \text{H.c.}) + J_{ij}\left(\boldsymbol{S}_i \cdot \boldsymbol{S}_j - \frac{1}{4} n_i n_j \right) \right] \mathcal{P}, \tag{7}$$

where $c_{i\sigma}$ is the annihilation operator of an electron with spin σ at site i, n_i is the number operator, and $\mathcal{P}$ is the projection operator to exclude double occupancy at each site. We assume that the parameters satisfy the following condition:

$$t_{ij} = J_{ij}/2 = tD(i-j)^{-2}. \tag{8}$$

This model is called the supersymmetric t-J model with an inverse-square interaction.[4] Here, the lattice constant is taken as the unit of length. Hence, the length L of the system gives also the number of lattice sites.

III. DENSITY MATRIX IN TERMS OF THE WAVE FUNCTION

We work with the electron density matrix $\rho_\sigma(x)$ for spin up $(\sigma=\uparrow)$ and spin down $(\sigma=\downarrow)$ electrons, which is the Fourier transform of the momentum distribution function $n_\sigma(k)$. Thus, we are interested in evaluating

$$\rho_\sigma(x) = \langle c_\sigma^\dagger(x + x_j) c_\sigma(x_j) \rangle \tag{9}$$

in the ground state. Here, we have written $c_\sigma(x_j)$ for $c_{j\sigma}$. The left-hand side of the equations is independent of x_j because of translational invariance. In Paper I, we have derived $\rho_\uparrow(x)$ analytically for a magnetization $m = n_\uparrow - n_\downarrow \geqslant 0$. The other part $\rho_\downarrow(x)$ requires a more elaborate calculation, which is presented in this paper.

For the down-spin part of the density matrix, we have to evaluate the expectation value in the ground state, with $M+1$ magnons and $Q-1$ holes, of

$$\rho_\downarrow(x) = \langle b_x^\dagger h_x h_0^\dagger b_0 \rangle = -\langle b_x^\dagger h_0^\dagger h_x b_0 \rangle + \delta_{x,0} \frac{M+1}{L} \equiv -G_\downarrow(x) + \delta_{x,0} \frac{M+1}{L}, \tag{10}$$

where the hole operators behave as fermionic. We will refer

to $G_\downarrow(x)$ as the propagator. Ignoring Kronecker's δ in the last expression, the expectation value forces one of the holes in the ket wave function to be at x and one of the magnons at the zeroth site, while in the bra wave function this is reversed. All other holes and magnons have to be matched in the bra and ket wave functions.

Using Eq. (4) with Eqs. (5) and (6), we use the normalization

$$B(M,Q) = \int \frac{dx_1}{L} \cdots \frac{dx_{M+Q}}{L} \Psi^2_{m+h}(z_1, \ldots, z_{M+Q}) \times \Psi^2_m(z_{Q+1}, \ldots, z_{M+Q}). \tag{11}$$

(Since Ψ_{m+h} and Ψ_h are products of real factors, a complex conjugation is not necessary.) Therefore, evaluating the expectation value in Eq. (10) in the ground state with $Q-1$ holes and $M+1$ magnons, we have

$$\langle b_x^\dagger h_0^\dagger h_x b_0 \rangle = \frac{1}{B(M+1,Q-1)} \frac{Q-1}{L} \frac{M+1}{L} \frac{(1-z_x)^2}{z_x} \int \frac{dx_2}{L} \cdots \frac{dx_{Q-1}}{L} \frac{dx_{Q+1}}{L} \cdots \frac{dx_{Q+M}}{L} \times \left(\prod_{i=2}^{Q-1} \frac{(1-z_i)(z_x-z_i)}{-z_i\sqrt{z_x}} \prod_{i=Q+1}^{Q+M} \frac{(1-z_i)(z_x-z_i)}{-z_i\sqrt{z_x}} \right)^2 \prod_{i=Q+1}^{Q+M} \frac{(z_x-z_i)(1-z_i)}{-z_i\sqrt{z_x}} \times \Psi^2_{m+h}(z_2, \ldots, z_{Q-1}, z_{Q+1}, \ldots, z_{M+Q}) \Psi^2_m(z_{Q+1}, \ldots, z_{M+Q}), \tag{12}$$

where $z_x = \exp(2\pi i x/L)$, and the factor $\Psi^2_{m+h}\Psi^2_m$ represents a system with $Q-2$ holes and M magnons. Equation (12) can be written in terms of the wave function for Q holes and M magnons, with the first two holes at the zeroth and x sites, as

$$G_\downarrow(x) = -\frac{1}{B(M+1,Q-1)} \frac{Q-1}{L} \frac{M+1}{L} \int \frac{dx_2}{L} \cdots \frac{dx_{Q-1}}{L} \frac{dx_{Q+1}}{L} \cdots \frac{dx_{Q+M}}{L} \prod_{i=Q+1}^{Q+M} \frac{(z_x-z_i)(z_i-1)}{z_i\sqrt{z_x}} \times \Psi^2_{m+h}(1, z_x, z_2, \ldots, z_{Q-1}, z_{Q+1}, \ldots, z_{M+Q}) \Psi^2_m(z_{Q+1}, \ldots, z_{M+Q}), \tag{13}$$

which further simplifies to

$$G_\downarrow(x) = -\frac{B(M,Q)}{B(M+1,Q-1)} \frac{Q-1}{L} \frac{M+1}{L} \times \left\langle (L\delta_{x_Q,0})(L\delta_{x_1,x}) \prod_{i=Q+1}^{Q+M} \frac{(z_x-z_i)(z_i-1)}{z_i\sqrt{z_x}} \right\rangle. \tag{14}$$

In this last expression, the expectation value is evaluated in the ground state with M magnons and Q holes, with hole coordinates at $z_1, \ldots, z_Q$ and magnon coordinates at $z_{Q+1}, \ldots, z_{Q+M}$. The factors of L associated with Kronecker's δ makes them $O(1)$ in the thermodynamic limit.

In Eq. (14), there is a factor for each magnon coordinate that can be expanded as

$$2\cos\phi - \exp[i\phi]/z_i - z_i \exp[-i\phi], \tag{15}$$

after defining $z_x = \exp[2i\phi]$ or $\phi = \pi x/L$. The product of each of these factors can, inside the expectation value of Eq. (14), be expressed as a sum of diagrams, similar to Paper I. This is pursued further in the next section.

IV. EVALUATION OF PROPAGATOR IN DIAGRAMS

A. Basics of the diagram technique

We first review how the normalization $B(M,Q)$ is evaluated. This discussion is almost identical to that in Ref. 11, but is reproduced here because it is essential in understanding the diagrammatic expansion. We make extensive use of a determinant representation of $|\Psi_G(\{z\})|^2$ following Ref. 5. We introduce a notation

$$\det_V(z_1, \ldots, z_Q) \equiv \det(z_1^p, \ldots, z_Q^p)_{p=-(Q-1)/2,\ldots,(Q-1)/2}, \tag{16}$$

where the suffix V means the Vandermonde determinant. In the matrix for the determinant, each row has an entry $(z_1^p, \ldots, z_Q^p)$, with $p=-(Q-1)/2$ in the first row and $p=(Q-1)/2$ in the Qth (last) row. Furthermore, the confluent alternant is introduced by

$$\det_A(z_1, \ldots, z_{M+Q}) \equiv \det(z_1^p, \ldots, z_Q^p, z_{Q+1}^p, pz_{Q+1}^p, \ldots, z_{M+Q}^p, pz_{M+Q}^p)_{p=-(2M+Q-1)/2,\ldots,(2M+Q-1)/2}. \tag{17}$$

It can be shown that $\det_A(z_1, \ldots, z_{M+Q})$ has fourth-order zeros $(z_i-z_j)^4$ if both z_i and z_j are magnon coordinates, second-order zeros $(z_i-z_j)^2$ if one of them is a hole coordinate, and first-order zeros (z_i-z_j) if both z_i and z_j are hole coordinates. Since Ψ_G in Eq. (2) and in Eq. (4) is real, we obtain up to a real positive factor,

$$|\Psi_G(\{z\})|^2 = \Psi_G(\{z\})^2 = (-1)^{P(M,Q)} \det_V(z_1, \ldots, z_Q) \det_A(z_1, \ldots, z_{M+Q}). \tag{18}$$

Here, $P(M,Q)=M(M-1)/2+(M+Q)(M+Q-1)/2$ comes from the factors of $(-i)$ in Eqs. (5) and (6). One can verify that there is no additional factor of (-1) from the determinants; taking the diagonal term from both determinants, which has a coefficient of +1, one obtains the lowest power possible for z_1, followed by the next lowest power for z_2, and so on. On the other hand, in the polynomials in Eqs. (5) and (6), since each (z_i-z_j) has $i<j$, this term is obtained by taking $-z_j$ from each such factor. Since each such factor in Ψ_G is repeated in Ψ_G^2, we have an overall coefficient of +1. The coefficient of this is therefore also +1, and there is no factor of (-1) in going from the polynomials to the determinants. Since $(-1)^n=1$ for any even n, $P(M,Q)$ is equivalent to $[Q^2+Q(2M-1)]/2 \equiv MQ+Q(Q-1)/2$.

Equation (11) can now be written as

$$B(M,Q) = (-1)^{P(M,Q)} \int \frac{dx_1}{L} \cdots \frac{dx_{M+Q}}{L} \times \det_V(z_1, z_2, \ldots, z_Q) \det_A(z_1, \ldots, z_{M+Q}). \tag{19}$$

The first determinant is a sum of terms of the form $z_1^{p_1} \cdots z_Q^{p_Q}$, and the second determinant is a sum of terms of the form $z_1^{q_1} \cdots z_Q^{q_Q} (p_{Q+1}-q_{Q+1}) z_{Q+1}^{p_{Q+1}+q_{Q+1}} \cdots (p_{Q+M}-q_{Q+M}) z_{Q+M}^{p_{Q+M}+q_{Q+M}}$, where $\{p_1, \ldots, p_Q\}$ is a permutation of $-(Q-1)/2, \ldots, (Q-1)/2$, and $\{q_1, \ldots, q_{Q+M}, p_{Q+1}, \ldots, p_{Q+M}\}$ is a permutation of $-(Q+2M-1)/2, \ldots, (Q+2M-1)/2$. We adopt the convention that $p_i > q_i$ for the magnons. Here, p_i's and q_i's are the momenta of the holes and magnons. Integrating the hole coordinates, $z_1, \ldots, z_Q$, we see that $p_i+q_i=0$; i.e., the p_i's and q_i's are equal and opposite, both covering the range $[-(Q-1)/2, (Q-1)/2]$. Now, integrating the magnon coordinates, $z_{Q+1}, \ldots, z_{M+Q}$, we see that $p_i+q_i=0$ for the magnons, too. Since the hole coordinates cover $[-(Q-1)/2, (Q-1)/2]$, the magnon p_i's range from $(Q+1)/2$ to $(Q+2M-1)/2$, and the minus sign counterpart.

Diagrammatically, $B(M,Q)$ can be represented as in Fig. 1, where $p_i+q_i=0$ forces all the lines to be horizontal. The holes are represented by the lines connecting black circles (from the Vandermonde determinant) to white circles (from the alternant), while the magnons are represented by lines connecting white circles to white circles. Every magnon line contributes a factor of p_i-q_i, i.e., its horizontal extent, while every hole line contributes a factor of unity. Various permutation symmetry factors have to be included to calculate $B(M,Q)$. The final result is

$$B(M,Q) = M!Q!(Q+1)(Q+3)\cdots(Q+2M-1). \tag{20}$$

As a result of this, Eq. (14) can be written as

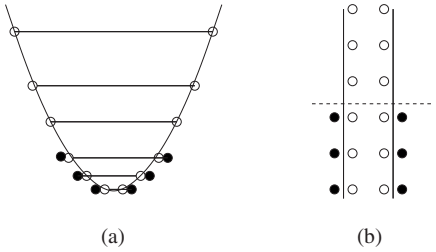

(a) (b)

FIG. 1. (a) Diagram for evaluating the product of Vandermonde and alternant determinants. The white circles denote the exponents in the alternant determinant, integer spaced from $-(Q+2M-1)/2$ to $(Q+2M-1)/2$. The horizontal positions of the circles give the exponents, which are equally spaced horizontally. The black circles denote the exponents in the Vandermonde determinant and are slightly separated from the white circles for clarity. A line connecting a black circle to a white one represents a hole coordinate, and one connecting a white circle to a white one represents a magnon coordinate. For clarity, some of the hole lines have not been shown: Every black circle should be connected to the white circle on the opposite side at the same level. (b) Schematic of the same diagram, where a vertical projection has been taken and the points are equally spaced on the vertical axis. The actual horizontal separation between two points can be calculated by counting how many levels down one side and up the other separate them. The dashed line is the magnon-hole boundary.

$$G_\downarrow(x) = -A(M,Q) \left\langle (L\delta_{x_Q,0})(L\delta_{x_1,x}) \times \prod_{i=Q+1}^{Q+M} (2\cos\phi - e^{i\phi}/z_i - z_i e^{-i\phi}) \right\rangle, \tag{21}$$

with

$$A(M,Q) = \frac{M+1}{L}\frac{Q-1}{L}\frac{B(M,Q)}{B(M+1,Q-1)} = \frac{Q(Q-1)}{L^2}\frac{(Q+1)(Q+3)\cdots(Q+2M-1)}{Q(Q+2)\cdots(Q+2M)}. \tag{22}$$

Expanding the product of factors in Eq. (21), for each magnon coordinate, we have a factor of $2\cos\phi$, $-\exp[i\phi]/z_i$ or its inverse. Therefore, in the diagrams contributing to the expectation value in Eq. (21), the total momentum for each magnon is 0 or ± 1, while the total momentum for each hole is still zero. Here, we have loosely referred these integers to "momentum," although physical momentum should be multiplied by $2\pi/L$. In addition, two of the holes—the first and the Q'th ones—have no constraint on their momentum because of Kronecker's δ in coordinate space. In Fig. 1, each magnon line connects two white circles, but can now be horizontal, ascending one step (going from left to right) or descending one step. Each hole line connects a black circle to a white circle, and is horizontal. However, for two of the holes, the black circle can connect to a white circle at any level. We refer to these hereafter as "jokers" because their momenta can assume any value. For

clarity, in subsequent figures, the black circles are replaced by hatched circles for the jokers. Note that if the joker at $x=x$ connects to a line that ascends n levels, it implies that the diagram has an overall factor of $z_x^n=\exp[2in\phi]$. On the other hand, for the joker at $x=0$, an ascending line yields a factor of unity. This is in contrast to the magnon lines, where an ascending line is associated with a factor of $\exp[i\phi]$, not $\exp[2i\phi]$. As discussed at the beginning of this section, each magnon line also contributes a factor equal to its total momentum.

As a warmup exercise, we evaluate $\langle(L\delta_{x_Q,1})(L\delta_{x_1,x})\times(2\cos\phi)^M\rangle$ in Eq. (21). All the magnon lines are horizontal and have the same contribution as in $B(M,Q)$. Therefore, either each joker connects to the white circle at its level, or the jokers exchange partners. In the first case, the momenta for both the jokers are zero, as in $B(M,Q)$. Instead of the sum over x_0 and x_Q, we have a factor of L with each Kronecker's δ, which has the same effect. In the second case, there is an extra factor of $-[\exp(2i\phi)]^{q_Q-q_1}$, where the (-1) factor comes from the permutation of terms within the determinants. The expectation value is therefore

$$\frac{(2\cos\phi)^M}{Q(Q-1)}\sum_{q_1\neq q_Q}[1-\exp(2i\phi)^{q_Q-q_1}], \tag{23}$$

which sums to

$$(2\cos\phi)^M\left[1-\frac{1}{Q(Q-1)}\left\{\frac{\sin^2 Q\phi}{\sin^2\phi}-Q\right\}\right]. \tag{24}$$

We are now in a position to evaluate the diagrams in Eq. (21). We classify the diagrams into four categories, in increasing order of complexity, and evaluate each of them. As in Ref. 11, we refer to the boundary between magnon and hole momenta in $B(M,Q)$ as the magnon-hole boundary, shown by a dashed line in Fig. 1, even though in a general diagram there can be magnon lines that go below this boundary and hole lines that go above this (for the holes that are the two jokers).

B. Type-I diagrams

In these diagrams, the jokers pair with the white circles at their own level or exchange partners. Therefore, neither joker connects to a white circle above the magnon-hole boundary. All the other holes have horizontal connections. This is a generalization of the diagrams just evaluated for $\langle(L\delta_{x_1,x})\times(L\delta_{x_Q,0})\rangle$, except that now the magnon lines need not be horizontal. Since all the hole lines stay below the magnon-hole boundary, the magnon lines have to stay above it. As explained in Ref. 11, each magnon line is either horizontal or exchanges partners with an adjacent magnon line to form a "dimer." As a result, the factor of $(2\cos\phi)^M$ changes to $F(M,Q)$, introduced in Paper I. $F(M,Q)$ describes the contribution of magnon pairs and dimers, and is defined by the recursion relation

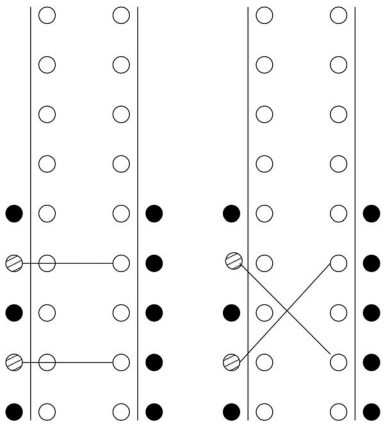

FIG. 2. Type-I diagrams. The jokers have shaded black circles. The two diagrams shown in the figure are a complementary pair. Both jokers are partnered with white circles below the magnon-hole boundary. All magnon lines are horizontal or dimerized.

$$F(M,Q)=2\cos\phi F(M-1,Q+2)-\{1+1/[(Q+2)^2-1]\}F(M-2,Q+4), \tag{25}$$

with the boundary conditions $F(0,Q+2M)=1$ and $F(1,Q+2M-2)=2\cos\phi$. From Eq. (24), the contribution to the propagator from type-I diagrams is then

$$G_{\rm I}(x)=-A(M,Q)F(M,Q)\left[1-\frac{1}{Q(Q-1)}\left\{\frac{\sin^2 Q\phi}{\sin^2\phi}-Q\right\}\right]. \tag{26}$$

The type-I diagrams (Fig. 2) can be divided into two complementary classes: For every diagram where the lines from the two jokers are horizontal, there is a corresponding diagram where their partners are exchanged. This generalizes to the subsequent, more complicated, classes of diagrams: Diagrams occur in complementary pairs, where the two diagrams in a pair differ in that the partners of the jokers are exchanged. The exchange of partners causes a factor of $-\exp[2i(q_Q-q_1)\phi]$, where q_Q-q_1 depends on the diagram. If $\phi=0$, the diagrams cancel each other, and all contributions to $G_\downarrow(x)$ are zero. This is reasonable since $G_\downarrow(x)$ involves destroying a hole and a magnon in the ground state, and the same site cannot have both a hole and a magnon.

C. Type-II diagrams

In these diagrams, one joker partners with a white circle above the magnon-hole boundary. The white circle that it would have paired with now has to be partnered. Recalling that, except for the jokers, holes must be linked with horizontal lines, this can happen in one of two ways. Either the other joker pairs with the white circle at its level, in which case the first joker must be just below the magnon-hole boundary, or the magnon line just above the boundary moves down one level. Alternatively, we have the same situation with the partners of the jokers exchanged. The two possibilities together are the complementary pair of diagrams just

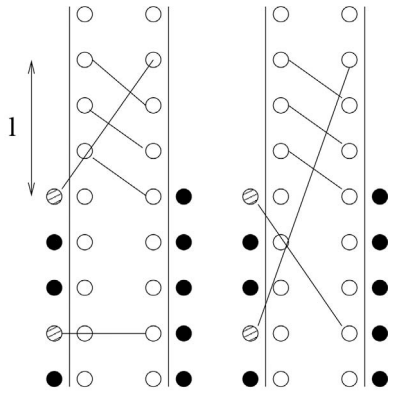

FIG. 3. Type-II diagrams. The jokers have shaded black circles. The two diagrams shown in the figure are a complementary pair. One joker is partnered with a white circle above the line l levels above the magnon-hole boundary. All magnon lines that are not shown are above this, and are horizontal or dimerized.

discussed, and are shown in Fig. 3. Since magnon lines can only have a total momentum of ±1 or 0, if the joker links to a circle l levels above the magnon-hole boundary, this affects the l magnons immediately above the boundary, as shown in the figure. Beyond the lth level, the magnon lines behave as before: They are horizontal or dimerized.

The contribution from these diagrams to the propagator is

$$G_{\mathrm{II}}(x) = -A(M,Q)\sum_{l=1}^{M}\frac{1}{Q}F(M-l,Q+2l)$$
$$\times\frac{Q}{Q+1}\frac{Q+2}{Q+3}\cdots\frac{Q+2l-2}{Q+2l-1}\Bigg[\exp(2il\phi)\exp(-il\phi)$$
$$\times\left\{1-\frac{1}{Q-1}\sum_{p=1}^{Q-1}\exp[-2i(l+p)\phi]\right\}$$
$$+\exp(il\phi)\exp(-2il\phi)\left\{1-\frac{1}{Q-1}\right.$$
$$\left.\times\sum_{p=1}^{Q-1}\exp[2i(l+p)\phi]\right\}+\phi\leftrightarrow-\phi\Bigg]. \quad (27)$$

The factors inside the summation are explained as follows. Let us first consider the case when the joker at $x=x$ is just below the left edge of the magnon-hole boundary, shown in the first panel in Fig. 3, and links to a white circle l levels above the magnon-hole boundary. The factor of $1/Q$ is because this joker could have occupied any of the Q black circles below the magnon-hole boundary and is now restricted to one position. The factor of $F(M-l,Q+2l)$ is because beyond the lth level above the magnon-hole boundary, the magnon lines are horizontal or dimerize as in type-I diagrams. The contribution from these magnons is as if the magnon-hole boundary was moved up by l levels. The factor of $Q/(Q+1)\cdots(Q+2l-2)/(Q+2l-1)$ is because each magnon line contributes a factor equal to its total momentum. The lowest l magnon lines, which are no longer horizontal,

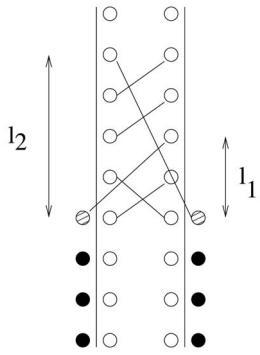

FIG. 4. Type-III diagrams. Both jokers are partnered with white circles above the line l_1 and l_2 levels above the magnon-hole boundary. All magnon lines that are not shown are below or above the $[l_1,l_2]$ block, and are horizontal or dimerized.

have each been reduced in total momentum by unity. The factor of $\exp(2il\phi)$ is because the joker at $x=x$ has a total momentum of l, resulting in a factor of $(z_x)^l=\exp(2il\phi)$. The factor of $\exp(-il\phi)$ comes because l magnon lines each have total momentum -1, from the Vandermonde and alternant determinants, so they must each have taken a factor of $-\exp(-i\phi)$ from Eq. (15), and there is an additional $(-1)^l$ permutation factor from the determinants because the line from the joker goes over l magnon lines it was previously under.

The next case is the group of diagrams complementary to the ones just considered, shown in the second panel in Fig. 3. This group gives rise to the second term inside the first $\{\}$ brackets in Eq. (27). If the second joker is p levels away from the first one, p is summed from 1 to $Q-1$, with a weighting factor of $1/(Q-1)$ for each. The total momentum of the first joker changes by $-(l+p)$ relative to the first diagram from the exchange of partners, resulting in a factor of $-\exp[-2i(l+p)\phi]$.

We also have to consider diagrams similar to these two classes, but in which the first joker is just below the right end of the magnon-hole boundary. Now, the total momentum of the joker is $-l$, and the l lowest magnon lines are ascending rather than descending. For the complementary diagrams, the total momentum of the first joker changes by $(l+p)$.

The remaining diagrams are similar to the four classes considered so far, except that the first joker is the one at $x=0$ rather than the one at $x=x$. It is possible to verify for each group separately that this changes ϕ to $-\phi$. All these contributions add up to Eq. (27). It is possible to verify that the $\phi\leftrightarrow-\phi$ is equivalent to an overall factor of 2.

The sums over p in Eq. (27) can be performed, yielding

$$G_{\mathrm{II}}(x) = -2A(M,Q)\sum_{l=1}^{M}F(M-l,Q+2l)$$
$$\times\frac{(Q+2)(Q+4)\cdots(Q+2l-2)}{(Q+1)(Q+3)\cdots(Q+2l-1)}\Bigg\{\exp(il\phi)$$
$$\times\left[1-\frac{\exp(iQ\phi)}{Q-1}\frac{\sin(Q-1)\phi}{\sin\phi}\right]+\phi\leftrightarrow-\phi\Bigg\}. \quad (28)$$

D. Type-III diagrams

Moving on in order of increasing complexity, we consider diagrams in which both jokers link to white circles above the magnon-hole boundary. The white circles they would have paired with need partners. For type-III diagrams, we assume that these partners come from above the magnon-hole boundary. This requires that both jokers should be immediately below the boundary. (For type-IV diagrams, we will assume that these two white circles pair with each other.) By an extension of the argument for type-II diagrams, both the jokers have to be immediately below the magnon-hole boundary, on either side of it. We assume that the jokers to the left and right pair with white circles l_1 and l_2 levels above the magnon-hole boundary, respectively. As seen in Fig. 4, both white circles immediately above the magnon-hole boundary connect to circles below the boundary, so that l_1 and l_2 have to be no less than 2. There is a block of ascending (for $l_2 > l_1$) or descending (for $l_1 > l_2$) magnon lines from $l_{\min}$ to $l_{\max}$, where $l_{\min}$ and $l_{\max}$ are the lesser and greater of l_1 and l_2, respectively. All other magnon lines are either horizontal or form dimers.

The total contribution to the propagator from type-III diagrams is

$$G_{\mathrm{III}}(x) = A(M,Q)\sum_{l_1=2}^{M}\sum_{l_2=2}^{M}\frac{1}{Q(Q-1)}F(l_{\min}-2,Q+2)F(M-l_{\max},Q+2l_{\max})\frac{Q^2}{Q+1}\frac{(Q+2l_{\min})(Q+2l_{\min}+2)\cdots(Q+2l_{\max}-2)}{(Q+2l_{\min}-1)(Q+2l_{\min}+1)\cdots(Q+2l_{\max}-1)}$$
$$\times\exp[i(l_2-l_1)\phi](\exp(2il_1\phi)\{1-\exp[-2i(Q-1+l_1+l_2)\phi]\}+\exp(-2il_2\phi)\{1-\exp[2i(Q-1+l_1+l_2)\phi]\}). \tag{29}$$

In this equation, there is a factor of (-1) from the permutation of the determinants, which cancels the (-1) in front. The $1/Q(Q-1)$ is because the location of the two jokers is fixed as being immediately below the magnon-hole boundary. The factors of F come from the dimerized magnon lines below $l_{\min}$ and above $l_{\max}$. The factors of $(Q+\text{const})$ are from the magnon lines: Instead of one line of length $Q+1$ immediately above the magnon-hole boundary, there are two lines of length Q that cross the boundary, and instead of $l_{\max}-l_{\min}+1$ horizontal magnon lines from the $l_{\min}$ to the $l_{\max}$ levels, there are $l_{\max}-l_{\min}$ ascending or descending lines. The ascending or descending lines also contribute l_2-l_1 factors of $-e^{i\phi}$ or l_1-l_2 factors of $-\exp[-i\phi]$, respectively; the (-1)'s are absorbed in the permutation factor at the beginning. The $\exp(2il_1\phi)$ comes from diagrams shown in Fig. 4, with the $x=x$ joker at the left end of the magnon-hole boundary. The complementary diagrams have an additional $-\exp[-2i(Q-1+l_1+l_2)\phi]$. The remaining terms are from the same diagrams, but with the $x=x$ joker at the right end of the magnon-hole boundary. Equation (29) simplifies to

$$G_{\mathrm{III}}(x) = A(M,Q)\sum_{l_1=2}^{M}\sum_{l_2=2}^{M}\frac{Q}{Q^2-1}F(l_{\min}-2,Q+2)\times F(M-l_{\max},Q+2l_{\max})\times\frac{(Q+2l_{\min})(Q+2l_{\min}+2)\cdots(Q+2l_{\max}-2)}{(Q+2l_{\min}-1)(Q+2l_{\min}+1)\cdots(Q+2l_{\max}-1)}\times\{2\cos[(l_1+l_2)\phi]-2\cos[(l_1+l_2+2Q-2)\phi]\}. \tag{30}$$

E. Type-IV diagrams

Finally, we come to diagrams where both jokers connect to white circles above the line, and the white circles they would have partnered with (i.e., at their level) pair with each other to form a magnon line. This is shown in Fig. 5. The two jokers now no longer have to be immediately below the magnon-hole boundary, but can be at any arbitrary depth below it. However, in order for their white circles to pair and form a magnon line, both jokers must be at the same level or differ in level by unity. The three possible cases are shown in Fig. 5. The contributions to the propagator from the first case is

$$G_{\mathrm{IV}_a}(x) = -A(M,Q)\sum_{p=0}^{Q/2-1}\sum_{l_1=1}^{M}\sum_{l_2=1}^{M}(2\cos\phi)\frac{1}{Q(Q-1)}\times F(l_{\min}-1,Q)F(M-l_{\max},Q+2l_{\max})(Q-1-2p)\times\frac{(Q+2l_{\min})\cdots(Q+2l_{\max}-2)}{(Q+2l_{\min}-1)\cdots(Q+2l_{\max}-1)}\times\exp[i(l_2-l_1)\phi](\exp[2i(l_1+p)\phi]\times\{1-\exp[-2i(l_1+l_2+Q-1)\phi]\}+\exp[-2i(l_2+p)\phi]\times\{1-\exp[2i(l_1+l_2+Q-1)\phi]\}). \tag{31}$$

This is similar to $G_{\mathrm{III}}(x)$, so we only discuss the differences. p is the number of levels below the magnon-hole boundary that the jokers are placed. The factor of $2\cos\phi$ comes from

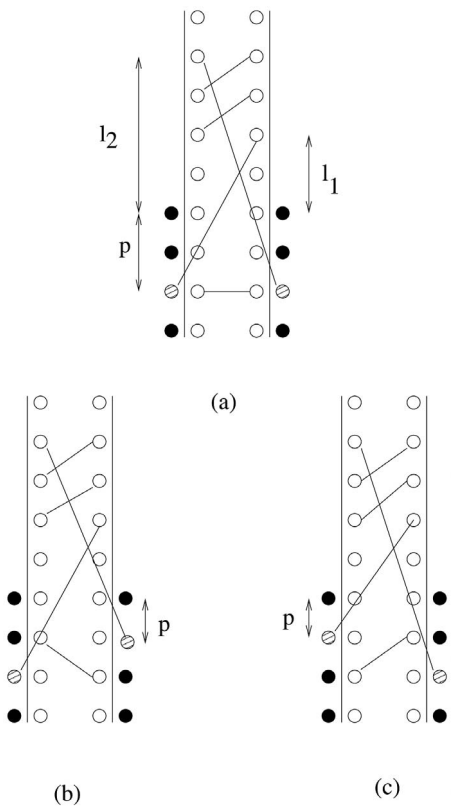

FIG. 5. Type-IV diagrams. Both jokers are partnered with white circles above the line l_1 and l_2 levels above the magnon-hole boundary. The white circles that they leave unpaired connect with each other, forming a magnon line below the magnon-hole boundary. This line must be horizontal, or ascending or descending by one level. All three cases are shown in the figure.

the magnon line below the magnon-hole boundary, as does the factor of $Q-1-2p$. The four terms within the brackets come from diagrams in the first panel of Fig. 5 with the $x=x$ joker on the left-hand side, the complementary group of diagrams, and the same with the $x=x$ joker on the right-hand side.

The contributions from the second and third cases are

$$G_{\mathrm{IV}_b}(x) = A(M,Q)\sum_{p=0}^{Q/2-2}\sum_{l_1=1}^{M}\sum_{l_2=1}^{M}\frac{1}{Q(Q-1)}F(l_{\min}-1,Q)$$
$$\times F(M-l_{\max},Q+2l_{\max})(Q-2-2p)$$
$$\times\frac{(Q+2l_{\min})\cdots(Q+2l_{\max}-2)}{(Q+2l_{\min}-1)\cdots(Q+2l_{\max}-1)}$$
$$\times\exp[i(l_2-l_1-1)\phi](\exp[2i(l_1+p+1)\phi]$$
$$\times\{1-\exp[-2i(l_1+l_2+Q-1)\phi]\}$$
$$+\exp[-2i(l_2+p)\phi]$$
$$\times\{1-\exp[2i(l_1+l_2+Q-1)\phi]\}) \quad (32)$$

and

$$G_{\mathrm{IV}_c}(x) = A(M,Q)\sum_{p=0}^{Q/2-2}\sum_{l_1=1}^{M}\sum_{l_2=1}^{M}\frac{1}{Q(Q-1)}F(l_{\min}-1,Q)$$
$$\times F(M-l_{\max},Q+2l_{\max})(Q-2-2p)$$
$$\times\frac{(Q+2l_{\min})\cdots(Q+2l_{\max}-2)}{(Q+2l_{\min}-1)\cdots(Q+2l_{\max}-1)}$$
$$\times\exp[i(l_2-l_1+1)\phi](\exp[2i(l_1+p)\phi]$$
$$\times\{1-\exp[-2i(l_1+l_2+Q-1)\phi]\}$$
$$+\exp[-2i(l_2+p+1)\phi]$$
$$\times\{1-\exp[2i(l_1+l_2+Q-1)\phi]\}). \quad (33)$$

Here, p is the distance of the joker that is closer to the magnon-hole boundary from the boundary. The differences between these and $G_{\mathrm{IV}a}$ can be explained. The sum over p stops at $Q/2-2$ because the lower joker is $p+1$ levels below the magnon-hole boundary. There is an overall minus sign relative to $G_{\mathrm{IV}a}$, which is a permutation factor. $2\cos\phi$ is replaced by $\exp(-i\phi)$ and $\exp(i\phi)$ because the magnon line below the magnon-hole boundary is descending or ascending instead of being horizontal. Finally, inside the brackets, we have $\exp[2i(l_1+p+1)\phi]$ in $G_{\mathrm{IV}b}$ because the joker on the left is l_1+p+1 levels below its partner, i.e., has a total momentum of l_1+p+1. (The $\exp[-2i(l_2+p+1)\phi]$ in $G_{\mathrm{IV}c}$ is similar.)

It is tedious but straightforward to carry out the sum over p in Eqs. (31)–(33). All three can be added up, and yield

$$G_{\mathrm{IV}}(x) = -A(M,Q)\sum_{l_1=1}^{M}\sum_{l_2=1}^{M}\frac{1}{Q}F(l_{\min}-1,Q)$$
$$\times F(M-l_{\max},Q+2l_{\max})$$
$$\times\frac{(Q+2l_{\min})\cdots(Q+2l_{\max}-2)}{(Q+2l_{\min}-1)\cdots(Q+2l_{\max}-1)}$$
$$\times\{2\cos[(l_1+l_2-1)\phi]$$
$$-2\cos[(l_1+l_2+2Q-1)\phi]\}. \quad (34)$$

V. THERMODYNAMIC LIMIT

A. Synthesis of all contributions to $G_\downarrow$

The expressions we have obtained for the various parts of $G_\downarrow(x)$ simplify in the thermodynamic limit $L\to\infty$. This limit makes $\phi\to 0$, but $Q\phi$ and $M\phi$ remain finite, and are given by

$$Q\phi = v_c x \quad (Q+2M)\phi = v_s x. \quad (35)$$

Here, we have fixed $Q/L=1-n$ and $M/L=(n-m)/2$, and used the velocities $v_c=\pi(1-n)$ for charge and $v_s=\pi(1-m)$ for spin. Elementary excitations with these velocities appear in the supersymmetric t-J model where both exchange and transfer decay as the inverse square of the distance.[4] Also, we obtain from Eq. (22) in the thermodynamic limit,

$$A(M,Q)\to\frac{Q}{L^2}\sqrt{\frac{Q}{Q+2M}}=\frac{1-n}{L}\sqrt{\frac{v_c}{v_s}} \quad (36)$$

and

$$\frac{(Q+2)\cdots(Q+2l-2)}{(Q+1)(Q+3)\cdots(Q+2l-1)} \to \frac{1}{\sqrt{(Q+1)(Q+2l-1)}} \tag{37}$$

if l/L is finite. Finally, from Ref. 11, in the thermodynamic limit,

$$F(M,Q) = \frac{\pi}{4}\sqrt{Q(Q+2M)}\left[Y_0\left(\frac{Q+2M}{2}\phi\right)J_0\left(\frac{Q}{2}\phi\right) - (J \leftrightarrow Y)\right] = \frac{\pi}{4}L^2\sqrt{v_c v_s}\left[Y_0\left(\frac{1}{2}v_s x\right)J_0\left(\frac{1}{2}v_c x\right) - J_0\left(\frac{1}{2}v_s x\right)Y_0\left(\frac{1}{2}v_c x\right)\right], \tag{38}$$

where J_ν and Y_ν are Bessel functions of νth order. Using Eqs. (36), (38), (37), and (26), we obtain in the thermodynamic limit

$$G_{\rm I}(x) \to -\frac{v_c^2}{4\pi}\left[Y_0\left(\frac{v_s}{2}x\right)J_0\left(\frac{v_c}{2}x\right) - J_0\left(\frac{v_s}{2}x\right)Y_0\left(\frac{v_c}{2}x\right)\right]\left(1-\frac{\sin^2 v_c x}{v_c^2 x^2}\right). \tag{39}$$

Next, we proceed to $G_{\rm II}(x)$. In Eq. (28), replacing the sum over l with an integral with $y=(l+Q/2)\phi$, and applying Eqs. (36), (38), and (37), we obtain in the thermodynamic limit

$$G_{\rm II}(x) \to -\frac{v_c}{\pi x}\Re\int_{v_c x/2}^{v_s x/2} dy\left[Y_0\left(\frac{v_s x}{2}\right)J_0(y)e^{iy} - (J \leftrightarrow Y)\right] \times\left[e^{-iv_c x/2} - e^{iv_c x/2}\frac{\sin v_c x}{v_c x}\right], \tag{40}$$

where $\Re$ takes the real part. Here, we have used the form for $F(M-l,Q+2l)$ that is valid if $(Q+2l)/L$ and $(M-l)/L$ are both finite in the thermodynamic limit. This is correct over essentially the entire range of l as $L\to\infty$. We see that the expressions in Eqs. (39) and (40) are finite in the thermodynamic limit. As given in Eq. (A2), we use the indefinite integral result

$$\int dy e^{iy}Z_0(y) = [Z_0(y) + iZ_0'(y)]ye^{iy}, \tag{41}$$

where $Z_0=J_0$ or Y_0 is a Bessel function of the zeroth order. Then, the integration of Eq. (40) results in

$$G_{\rm II}(x) = -\frac{2v_c}{\pi^2 x}\left[\sin\frac{v_s-v_c}{2}x - \sin\frac{v_s+v_c}{2}x\frac{\sin v_c x}{v_c x}\right] + \frac{v_c^2}{2\pi}\left[Y_0\left(\frac{v_s x}{2}\right)J_0\left(\frac{v_c x}{2}\right) - J_0\left(\frac{v_s x}{2}\right)Y_0\left(\frac{v_c x}{2}\right)\right] \times\left(1-\frac{\sin v_c x\cos v_c x}{v_c x}\right) - \frac{v_c\sin^2(v_c x)}{2\pi x} \times\left[Y_0\left(\frac{v_s x}{2}\right)J_1\left(\frac{v_c x}{2}\right) - J_0\left(\frac{v_s x}{2}\right)Y_1\left(\frac{v_c x}{2}\right)\right], \tag{42}$$

where we have used the relation $J_0'(y)=-J_1(y)$ and $Y_0'(y)=-Y_1(y)$ given by Eq. (A2) and the simple Wronskian given by Eq. (A1).

We continue on to the evaluation of $G_{\rm III}(x)$ and $G_{\rm IV}(x)$, which are more complicated. From Eqs. (30) and (34), the thermodynamic limits of both $G_{\rm III}(x)$ and $G_{\rm IV}(x)$ are infinite: $A(M,Q)$ is $O(1/L)$, the two F functions are both $O(L)$ if all their arguments are $O(L)$, as they generically are, and the polynomials in Q in the numerator and denominator have an overall $O(1/L^2)$ behavior. The double sum, over l_1 and l_2, makes $G_{\rm III}(x)$ and $G_{\rm IV}(x)$ of $O(L)$. However, $G_{\rm III}$ and $G_{\rm IV}$ almost exactly cancel each other, and their difference is finite in the thermodynamic limit. Comparing Eqs. (30) and (34), we see that $G_{\rm III}(x)$ and $G_{\rm IV}(x)$ are equal and opposite, except for four differences: (i) The sums over l_1 and l_2 have different ranges, (ii) the polynomials in Q in the numerator and denominator are different, (iii) the arguments of the first F function are different, and (iv) the arguments of the cosines in the brackets are different. Of these, (i) and (ii) cause a negligible difference in the thermodynamic limit, but (iii) and (iv) are significant. We consider the effects of all four separately.

First, if $l_1=1$, a term that exists in $G_{\rm IV}(x)$ but not in $G_{\rm III}(x)$, there is no $O(L)$ factor from the sum over l_1, and $F(0,Q)=1$ instead of being $O(L)$. Therefore, the contribution of this term to $G_{\rm IV}(x)$ is $O(1/L)$ and can be neglected. The same is true for $l_2=1$. Second, there is a factor of $Q/(Q^2-1)$ in $G_{\rm III}$ instead of $1/Q$ in $G_{\rm IV}$. This is equal to $(1/Q)[1+1/Q^2+O(1/Q^4)]$. The correction from this is $G_{\rm III}(x)/Q^2$, which is $O(1/L)$ in the thermodynamic limit and can be neglected.

To account for the difference (iii), we note that the contribution for the sum of $G_{\rm III}$ and $G_{\rm IV}$ contains the term

$$F(M-l_1,Q+2l_1)[F(l_2-2,Q+2)-F(l_2-1,Q)], \tag{43}$$

where we have taken $l_{\min}=l_2$ and $l_{\max}=l_1$ without loss of generality. In the thermodynamic limit, the difference ΔF of the two F's is given by

$$\Delta F = -\frac{\pi}{4}\sqrt{\frac{2y_2}{v_c}}\left\{\left[Y_0\left(\frac{1}{2}v_c x\right)J_0(y_2) - (J \leftrightarrow Y)\right] + v_c x\left[Y_0\left(\frac{1}{2}v_c x\right)J_0'(y_2) - (J \leftrightarrow Y)\right]\right\}, \tag{44}$$

where $y_2=(Q/2+l_2)\phi$. Then, the whole contribution from (iii) is given by

$$G_a(x) \equiv \frac{\pi^2}{4L^2}\sum_{l_1=1}^{M}\sum_{l_2=1}^{l_1}\left[Y_0\left(\frac{1}{2}v_s x\right)J_0(y_1) - (J \leftrightarrow Y)\right]\left\{ Y_0(y_2) \times\left[J_0\left(\frac{1}{2}v_c x\right) + v_c x J_0'\left(\frac{1}{2}v_c x\right)\right] - (J \leftrightarrow Y)\right\}\Re e^{i(y_1+y_2)} \times(e^{-iv_c x} - e^{iv_c x}), \tag{45}$$

where $y_1=(Q+l_1/2)\phi$. Replacing the sums with integrals over y_1 and y_2, we obtain

$$G_a(x)=\frac{\sin(v_c x)}{2x^2}\Im\int_{v_c x/2}^{v_s x/2}dy_1\int_{v_c x/2}^{y_1}dy_2\left[Y_0\left(\frac{1}{2}v_s x\right)\times J_0(y_1)e^{iy_1}-(J\leftrightarrow Y)\right]\left\{\left[J_0\left(\frac{1}{2}v_c x\right)+v_c x J_0'\left(\frac{1}{2}v_c x\right)\right]\times Y_0(y_2)e^{iy_2}-(J\leftrightarrow Y)\right\}, \tag{46}$$

where $\Im$ takes the imaginary part. Finally, the effect (iv) of the change in the argument of the cosines is to differentiate them, since $\phi\to 0$, yielding

$$G_b(x)\equiv-\frac{\pi^2 v_c x}{4L^2}\sum_{l_1=1}^{M}\sum_{l_2=1}^{l_1}\left[Y_0\left(\frac{1}{2}v_s x\right)J_0(y_1)-(J\leftrightarrow Y)\right]\times\left[Y_0(y_2)J_0\left(\frac{1}{2}v_c x\right)-(J\leftrightarrow Y)\right]\Im e^{i(y_1+y_2)}\times(e^{-iv_c x}+e^{iv_c x}). \tag{47}$$

As in the case of G_a, replacing the sums with integrals over y_1 and y_2, we obtain

$$G_b(x)=\frac{v_c\cos(v_c x)}{2x}\Im\int_{v_c x/2}^{v_s x/2}dy_1\int_{v_c x/2}^{y_1}dy_2\left[Y_0\left(\frac{v_s}{2}x\right)J_0(y_1)e^{iy_1}-(J\leftrightarrow Y)\right]\left[Y_0\left(\frac{v_c}{2}x\right)J_0(y_2)e^{iy_2}-(J\leftrightarrow Y)\right]. \tag{48}$$

Then, we obtain the thermodynamic limit of $G_{\mathrm{III}}(x)+G_{\mathrm{IV}}(x)=G_a(x)+G_b(x)$.

In Eqs. (46) and (48), the integration over y_1 and y_2 can be performed analytically by the use of Eq. (41). The integral over y_2 has the upper limit y_1 and the lower limit $v_c x/2$. Surprisingly, the contribution from the lower limit cancels out $G_{\mathrm{II}}(x)$ exactly. The final integration over y_1 with terms coming from the upper limit $y_2=y_1$ can be carried out by using the following formula, which are derived in the Appendix:

$$I_{JJ}\equiv\int_{v_c x/2}^{v_s x/2}dy\,yJ_0(y)[J_0(y)\sin 2y-J_1(y)\cos 2y]=\frac{1}{2}\Im\{[J_0(y)-iJ_1(y)]^2y^2e^{i2y}\}\Big|_{v_c x/2}^{v_s x/2}, \tag{49}$$

$$I_{YY}\equiv\int_{v_c x/2}^{v_s x/2}dy\,yY_0(y)[Y_0(y)\sin 2y-Y_1(y)\cos 2y]=\frac{1}{2}\Im\{[Y_0(y)-iY_1(y)]^2y^2e^{i2y}\}\Big|_{v_c x/2}^{v_s x/2}, \tag{50}$$

$$I_{JY}\equiv\int_{v_c x/2}^{v_s x/2}dy\,yJ_0(y)[Y_0(y)\sin 2y-Y_1(y)\cos 2y]=\frac{1}{2}\Im\{[J_0(y)-iJ_1(y)][Y_0(y)-iY_1(y)]y^2e^{i2y}\}\Big|_{v_c x/2}^{v_s x/2}+\frac{\sin v_s x-\sin v_c x}{2\pi}, \tag{51}$$

$$I_{YJ}\equiv\int_{v_c x/2}^{v_s x/2}dy\,yY_0(y)[J_0(y)\sin 2y-J_1(y)\cos 2y]=\frac{1}{2}\Im\{[Y_0(y)-iY_1(y)][J_0(y)-iJ_1(y)]y^2e^{i2y}\}\Big|_{v_c x/2}^{v_s x/2}-\frac{\sin v_s x-\sin v_c x}{2\pi}. \tag{52}$$

Collecting the terms, we find tremendous cancellation. Furthermore, many combinations take the form of the Wronskian equation [Eq. (A1)], and can be simplified. The propagator $G_\downarrow(x)=G_{\mathrm{I}}(x)+G_{\mathrm{II}}(x)+G_a(x)+G_b(x)$ is now given a closed form:

$$\begin{aligned}G_\downarrow(x)=&-\frac{1}{4\pi x^2}[v_c x\cos(v_c x)-\sin(v_c x)][v_s x\cos(v_s x)-\sin(v_s x)]\left[J_0\left(\frac{1}{2}v_s x\right)Y_0\left(\frac{1}{2}v_c x\right)-Y_0\left(\frac{1}{2}v_s x\right)J_0\left(\frac{1}{2}v_c x\right)\right]\\&-\frac{1}{4\pi}v_c\sin(v_c x)v_s\sin(v_s x)\left[J_1\left(\frac{1}{2}v_s x\right)Y_1\left(\frac{1}{2}v_c x\right)-Y_1\left(\frac{1}{2}v_s x\right)J_1\left(\frac{1}{2}v_c x\right)\right]\\&+\frac{1}{4\pi x}v_c\sin(v_c x)[\sin(v_s x)-v_s x\cos(v_s x)]\left[J_0\left(\frac{1}{2}v_s x\right)Y_1\left(\frac{1}{2}v_c x\right)-Y_0\left(\frac{1}{2}v_s x\right)J_1\left(\frac{1}{2}v_c x\right)\right]\\&-\frac{1}{4\pi x}v_s\sin(v_s x)[\sin(v_c x)-v_c x\cos(v_c x)]\left[J_0\left(\frac{1}{2}v_c x\right)Y_1\left(\frac{1}{2}v_s x\right)-Y_0\left(\frac{1}{2}v_c x\right)J_1\left(\frac{1}{2}v_s x\right)\right].\end{aligned} \tag{53}$$

This is the main result of the present paper.

Figure 6 shows $G_\downarrow(x)$ for a few cases of n with m fixed as 0.1. In order to test the results, we have also computed the inverse Fourier transform of Ref. 8 to the real space, as shown by dots. The agreement between the present calculation and Ref. 8 is excellent. Although the curves in Fig. 6 are shown as continuous, and all pass through the origin because $G_\downarrow(x\to 0)=0$ from Eq. (53), the coordinate x is only

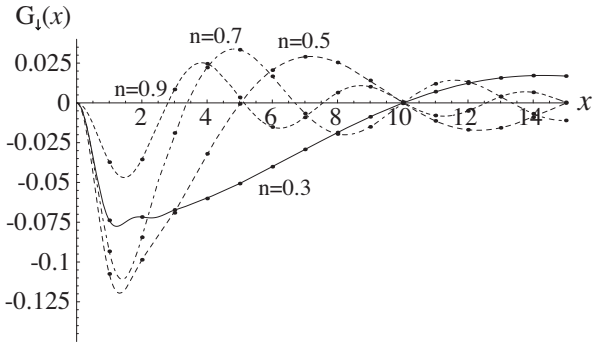

FIG. 6. Distance dependence of $G_{\downarrow}(x)=-\rho_{\downarrow}(x)+\delta_{x,0}(n-m)/2$, with $n=0.9,0.7,0.5,0.3$ and $m=0.1$ for all cases. Only integer values of x are physically relevant. For comparison, the data obtained by the inverse Fourier transform of Kollar-Vollhardt results are also shown by points. A wriggle for $1<x<2$ in the case of $n=0.3$ comes from the analytic form of Eq. (53), but only integer values of x are physically relevant. The wriggles between integer valus of x in the ensuing figures are of the same character.

physical for integer x. This point will next be discussed in detail.

B. Comparison between $G_{\uparrow}$ and $G_{\downarrow}$

The up-spin density matrix is related to the propagator $G_{\uparrow}(x)=\langle h_0^{\dagger}h_x\rangle$ introduced in Paper I as

$$\rho_{\uparrow}(x) \equiv \langle c_{\uparrow}^{\dagger}(x+x_j)c_{\uparrow}(x_j)\rangle = \delta_{x,0}\left[1-\frac{1}{2}(n-m)\right]-G_{\uparrow}(x). \tag{54}$$

From the definition, we obtain $G_{\uparrow}(x=0)=1-n$ and $\rho_{\uparrow}(x=0)=(n+m)/2$. On the other hand, using Eq. (10), we obtain $\rho_{\downarrow}(x=0)=(n-m)/2$ and $G_{\downarrow}(x=0)=0$. We note that $G_{\sigma}(x=0)=G_{\sigma}(x\to 0)$ for both up and down spins despite the fact that only integer values of x are physical.

In the singlet case $m=0$, the up- and down-spin density matrices should coincide. This implies that $G_{\downarrow}(x;m=0)=G_{\uparrow}(x;m=0)$ for $x\neq 0$, but

$$G_{\downarrow}(x=0;m=0) \neq G_{\uparrow}(x=0;m=0) \tag{55}$$

because of a difference in Kronecker's δ terms. Let us see how these relations appear in our result. At $v_s=\pi$, which happens for $m=0$, $G_{\downarrow}(x;m=0)$ with integer $x(\neq 0)$ simplifies to

$$G_{\downarrow}^{(r)}(x) = \frac{v_c(-1)^x}{4}\left[\left\{\cos(v_c x)-\frac{\sin(v_c x)}{v_c x}\right\}\left\{Y_0\left(\frac{v_s x}{2}\right)J_0\left(\frac{v_c x}{2}\right) - J_0\left(\frac{v_s x}{2}\right)Y_0\left(\frac{v_c x}{2}\right)\right\} + \sin(v_c x)\left\{Y_0\left(\frac{v_s x}{2}\right)J_1\left(\frac{v_c x}{2}\right) - J_0\left(\frac{v_s x}{2}\right)Y_1\left(\frac{v_c x}{2}\right)\right\}\right], \tag{56}$$

where the superscript in $G_{\downarrow}^{(r)}$ signifies that this reduced form is only valid for $m=0$ and integer $x\neq 0$. This indeed agrees

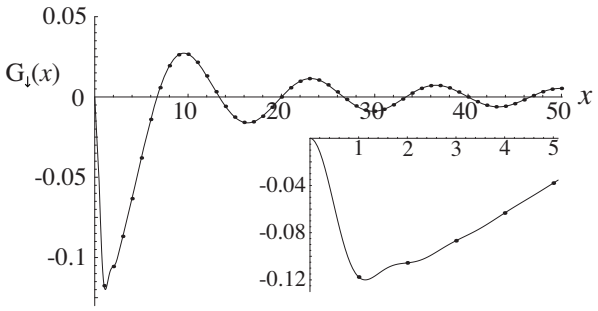

FIG. 7. Distance dependence of $G_{\downarrow}(x)$ in the singlet limit with $n=0.3$ and $m=0$ (solid line and dots). The inset shows the expanded view for small x.

with the result in Paper I for $G_{\uparrow}$ with $m=0$. Thus, the present calculation and the previous one consistently cover the whole range of magnetization.

Figure 7 shows the result for $G_{\downarrow}(x)$ given by Eq. (53), with $n=0.3$ and $m=0$. The result for noninteger values of x is included to clarify the analytic property, especially for a small x. The curve for $x>1$ tends to the value $-\rho_{\downarrow}(0)=-n/2=-0.15$, but finally goes to zero in the limit $x\to 0$, as discussed in Fig. 6. The period Δx of damped oscillation is given by $\Delta x\sim 4/n\sim 13$. One might naively expect from the trigonometric function in Eq. (56) that

$$\Delta x \overset{?}{=} \frac{2\pi}{v_c} = \frac{4}{1-n}, \tag{57}$$

which is not the case. This situation becomes clearer in Fig. 8, which shows the result for a very dilute density $n=0.1$. Since the electron correlation is not important except for small x, the result for $G_{\downarrow}(x)$ is well fitted by the noninteracting result: $G(x)=-\sin(\pi n x/2)/(\pi x)$. However, the hard-core constraint causes deviation from the noninteracting behavior near $x=0$. The period of damped oscillation is determined by the Fermi momentum $k_F=\pi n/2$, which is the same as the Fermi velocity in our unit. The Fermi velocity determines the principal oscillation for a general case of n such as $n=0.3$.

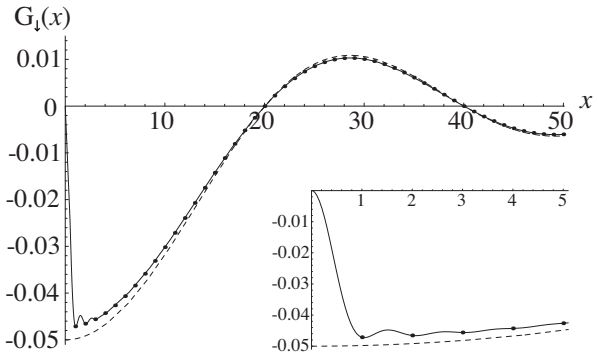

FIG. 8. Distance dependence of $G_{\downarrow}(x)$ in the singlet limit with $n=0.1$ and $m=0$ (solid line and dots). The shape is reasonably well fitted by $-\sin(\pi n x/2)/(\pi x)$ (dashed line), which is the case for noninteracting electrons. The inset shows the expanded view for small x.

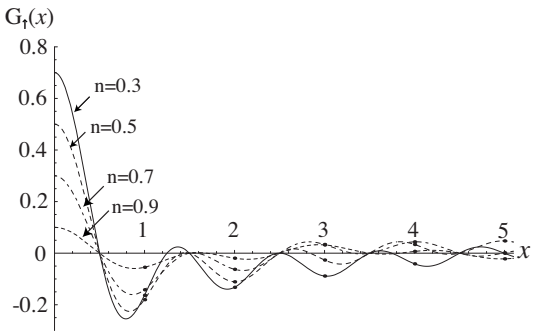

FIG. 9. Distance dependence of $G_\uparrow(x)$ with $n=0.9,0.7,0.5,0.3$ and $m=0.1$ for all cases. Only integer values of x are physically relevant, and the lines are shown only for easy tracking of $G_\uparrow(x)$ at integers.

For a comparison between $G_\uparrow$ and $G_\downarrow$, Fig. 9 shows $G_\uparrow(x)$ given by

$$G_\uparrow(x) = \frac{v_c \cos(\pi x)}{4}\left[\left(\cos(v_c x) - \frac{\sin(v_c x)}{v_c x}\right)\right.$$
$$\times\left\{Y_0\left(\frac{v_s x}{2}\right)J_0\left(\frac{v_c x}{2}\right) - J_0\left(\frac{v_s x}{2}\right)Y_0\left(\frac{v_c x}{2}\right)\right\}$$
$$+ \sin(v_c x)$$
$$\left.\times\left\{Y_0\left(\frac{v_s x}{2}\right)J_1\left(\frac{v_c x}{2}\right) - J_0\left(\frac{v_s x}{2}\right)Y_1\left(\frac{v_c x}{2}\right)\right\}\right], \tag{58}$$

where $\cos(\pi x)$ is used instead of $(-1)^x$ used in Paper I, in order to include noninteger values of x. The main difference from $G_\downarrow(x)$ is the finite limiting value of $1-n$ as $x\to 0$. There are also oscillations between neighboring integer values of x, unlike for $G_\downarrow(x)$, but these are not physical. We note that after replacing $(-1)^x$ with $\cos(\pi x)$, $G_\downarrow^{(r)}(x)$ is the same as $G_\uparrow(x)$, and therefore has the same nonzero $x\to 0$ limit and oscillations, emphasizing the limited equivalence between $G_\downarrow^{(r)}(x)$ and $G_\uparrow(x)$.

C. Asymptotic behavior

The long-distance behavior of the propagator shows the singularity of the momentum distribution, as discussed in Paper I. Using the known asymptotic form of the Bessel functions, and using the Fermi velocities $k_{F\uparrow}=\pi(n+m)/2$ and $k_{F\downarrow}=\pi(n-m)/2$, we have derived the leading behavior of $G_\downarrow(x)$ for large x as

$$G_\downarrow(x) \sim \frac{-1}{\pi x}\sqrt{(1-n)(1-m)}\left[\sin k_{F\downarrow}x - \frac{n_\downarrow \cos k_{F\downarrow}x}{2\pi(1-n)(1-m)x}\right.$$
$$- \frac{(n-m)^2}{32\pi^2(1-m)^2(1-n)^2x^2}\sin k_{F\downarrow}x$$
$$\left. + \frac{\sin[(2k_{F\uparrow}+k_{F\downarrow})x]}{4\pi^2(1-n)^2x^2} - \frac{\sin[(2k_{F\uparrow}-k_{F\downarrow})x]}{4\pi^2(1-m)^2x^2}\right] \tag{59}$$

up to $O(1/x^3)$. For reference, our previous result in Paper I for the up spin is quoted[14] to $O(1/x^3)$ as

$$G_\uparrow(x) \sim \frac{-1}{\pi x}\sqrt{\frac{1-n}{1-m}}\left[\sin k_{F\uparrow}x - \frac{n_\downarrow \cos k_{F\uparrow}x}{2\pi(1-n)(1-m)x}\right.$$
$$\left. - \frac{1+n_\downarrow^2/[2(1-n)^2]}{4\pi^2(1-m)^2x^2}\sin k_{F\uparrow}x + \frac{\sin(k_{F\uparrow}+2k_{F\downarrow})x}{4\pi^2(1-n)^2x^2}\right]. \tag{60}$$

In the case of singlet $m=0$, the present result [Eq. (59)] agrees with Eq. (60).

D. Singularities in momentum distribution

The momentum distribution $n_\downarrow(k)$ is obtained from the Fourier transform of $G_\downarrow(x)$ as

$$n_\downarrow(k) = \frac{1}{2}(n-m) - \sum_{x=-L/2}^{L/2} G_\downarrow(x)\cos kx. \tag{61}$$

An $\exp(ik_0x)/x^{p+1}$ term in $G_\downarrow(x)$ corresponds to a discontinuity in the pth derivative of $n_\downarrow(k)$ at $k=k_0$. Thus, $n_\downarrow(k)$ and its derivatives are discontinuous at $k=\pm k_{F\downarrow}$. In addition, the second and higher derivatives of $n_\downarrow(k)$ are discontinuous at $|k|=|k_{F\downarrow}\pm 2k_{F\uparrow}|$. The discontinuity at $k=k_{F\downarrow}$ is derived from Eq. (59) as

$$\Delta n_\downarrow(k_{F\downarrow}) \equiv n_\downarrow(k_{F\downarrow}+0) - n_\downarrow(k_{F\downarrow}-0) = -\sqrt{(1-n)(1-m)}, \tag{62}$$

while the up-spin discontinuity is given in Paper I as

$$\Delta n_\uparrow(k_{F\uparrow}) = -\sqrt{(1-n)/(1-m)}, \tag{63}$$

which agrees with $\Delta n_\downarrow(k_{F\downarrow})$, with $m=0$. Note that the majority spin $(\uparrow)$ has a larger discontinuity, giving $\Delta n_\uparrow(k_{F\uparrow})=1$ in the case of full polarization $m=n$. This must be the case since the system becomes the same as free fermions without spin. The next singularity is the discontinuity in the slope, which is on top of $\Delta n_\downarrow(k_{F\downarrow})$ and is given by

$$\Delta\left(\frac{dn_\downarrow(k_{F\downarrow})}{dk}\right) = \frac{n_\downarrow}{2\pi(1-n)^{1/2}(1-m)^{1/2}}. \tag{64}$$

Furthermore, the discontinuities in the curvature are obtained from Eq. (59) as

$$\Delta\left(\frac{d^2n_\downarrow(2k_{F\uparrow}+k_{F\downarrow})}{dk^2}\right) = +\frac{\sqrt{1-m}}{4\pi^2(1-n)^{3/2}}, \tag{65}$$

$$\Delta\left(\frac{d^2n_\downarrow(2k_{F\uparrow}-k_{F\downarrow})}{dk^2}\right) = -\frac{\sqrt{1-n}}{4\pi^2(1-m)^{3/2}}. \tag{66}$$

In the case of singlet $m=0$, Eq. (65) corresponds to the momentum $k=3k_F$, while Eq. (66) contributes to the discontinuity in the curvature at $k=k_F$. On the other hand, we have obtained the following in Paper I:

$$\Delta\left(\frac{d^2n_\uparrow(k_{F\uparrow}+2k_{F\downarrow})}{dk^2}\right) = \frac{1}{4\pi^2(1-n)^{3/2}(1-m)^{1/2}}. \tag{67}$$

Equations (67) and (65) are reduced to the same with $m=0$.

Note that there is no singularity in $n_\uparrow(k)$ at $k=\pm(k_{F\uparrow}-2k_{F\downarrow})$, while there is one in $n_\downarrow(k)$ at $k=\pm(k_{F\downarrow}-2k_{F\uparrow})$. This curious asymmetry between up and down spins can be understood by appealing to elementary excitations in the supersymmetric t-J model.[4,9,15] Namely, the fermionic excitations are combinations of charge excitations (holons and antiholons) and spin excitations (spinons and antispinons). The threshold momentum and the quantum number for each gapless excitation is given by[15,16]

$$\text{spinon}: \pm \pi m/2, \quad \text{with spin } 1/2,$$
$$\text{antispinon}: \pm \pi m, \quad \text{with spin } 1, \tag{68}$$

$$\text{holon}: \pm \pi n/2, \quad \text{with charge} + 1,$$
$$\text{antiholon}: \pm \pi n, \quad \text{with charge} - 2. \tag{69}$$

The simplest is a holon-spinon excitation, which makes up a fermionic hole. The excitation gives the characteristic momenta, $\pm k_{F\uparrow}=\pm\pi(n+m)/2$ and $\pm k_{F\downarrow}=\pm\pi(n-m)/2$.

On the other hand, an electron addition excitation has the charge -1 and must involve an antiholon. The simplest combination consists of

$$(\text{holon}) + (\text{spinon}) + (\text{antiholon}). \tag{70}$$

The threshold momenta are not only $\pm k_F$ but also those that are reduced to $\pm 3k_F$ in the singlet limit. For example, we obtain

$$\pi n/2 + \pi m/2 + \pi n = \pi n/2 - \pi m/2 + 2\pi(n+m)/2$$
$$= k_{F\downarrow} + 2k_{F\uparrow}. \tag{71}$$

Furthermore, the combination (holon)+(spinon)+(antispinon) can also make up a hole excitation with positive charge. However the spin can take only the value $+1/2$ since the antispinon excitation from the magnon condensate accompanies the spin flip from down to up, but not the opposite. Because $n_\uparrow(k)=\langle c_{k\uparrow}^\dagger c_{k\uparrow}\rangle$ involves hole excitations with spin $-1/2$ as a result of acting $c_{k\uparrow}$ to the ground state, the antispinon cannot participate in the process. In $n_\downarrow(k)$, on the other hand, excitations accompany the spin change $+1/2$ by $c_{k\downarrow}$. Then, a threshold momentum is given by

$$-\pi n/2 - \pi m/2 - \pi m = \pi(n-m)/2 - 2\pi(n+m)/2$$
$$= k_{F\downarrow} - 2k_{F\uparrow}. \tag{72}$$

Hence, there emerges a weak singularity at this momentum and the minus sign counterpart.

In order to see the global behavior in the momentum space, we numerically carry out the Fourier transform of $G_\downarrow(x)$ and derive the momentum distribution function $n_\downarrow(k)$. The analytic calculation also seems possible, but is extremely complicated.[17] In this paper, we are satisfied with a numerical comparison with previous results.[8] As shown in Fig. 10, the agreement between the present and previous results is excellent. It is difficult to identify the tiny discontinuities in the curvature at $k_{F\downarrow}-2k_{F\uparrow}$ in Fig. 10. However, the discontinuity in the slope at $k_{F\downarrow}$ is clearly seen and is characterized by Eq. (64).

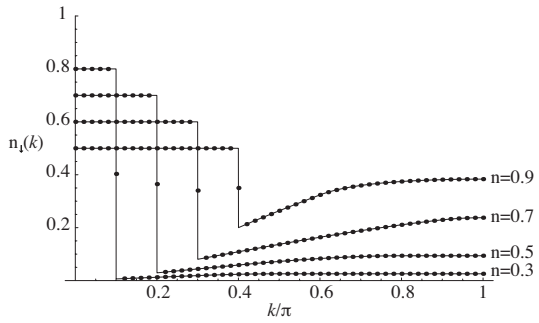

FIG. 10. Plot of $n_\downarrow(k)$ versus k with $n=0.9, 0.7, 0.5, 0.3$ and $m=0.1$ for all cases. For comparison, the Kollar-Vollhardt results (Ref. 8) are also shown by solid lines.

VI. CONCLUDING REMARKS

We have obtained the analytic form of the density matrix of the Gutzwiller wave function with allowance of magnetization. Together with the previous results for the majority spin, we now have expressions for both components of spins. The density matrix in the thermodynamic limit is characterized by spin and charge velocities, which represent elementary excitations in the supersymmetric t-J model with inverse-square exchange and transfer.[4,15,16] The singularities in the momentum distribution are identified completely. The identification through the asymptotic form of the density matrix is more effective than previous methods,[18] which try to analyze them in the momentum space.

Although we have dealt with many complicated terms, the final result seems relatively simple, as given by Eq. (53). The simplification emerges only in the thermodynamic limit. A similar simplification has also been seen in the exact dynamics, where an extremely complicated expression for finite size leads to a final result in terms of simple form factors.[9] In the present case, even after the thermodynamic limit is taken, there is considerable further simplification, with double integrals involving products of four Bessel functions eventually reducing to Eq. (53). It is tempting to speculate that there may be a way to work directly in the thermodynamic limit without bothering about finite size, or even to obtain a completely different real space formulation in which the final results are obtained without "fortuitous" cancellations.

ACKNOWLEDGMENTS

M.A. is supported by the University of Tsukuba Research Initiative. Parts of the numerical calculations were carried out on the computers at YITP in Kyoto University.

APPENDIX: IDENTITIES INVOLVING BESSEL FUNCTIONS

Here, we summarize the properties of Bessel functions, which are used in this paper. Bessel functions have the simple Wronskian,

$$J_0(x)Y_0'(x) - J_0'(x)Y_0(x) = \frac{2}{\pi x}, \tag{A1}$$

which comes from Abel's identity. Another important property is the differentials,

$$Z_0'(x) = -Z_1(x), \quad Z_1'(x) = Z_0(x) - \frac{1}{x}Z_1(x), \tag{A2}$$

which apply for cases $Z_\nu(x)=J_\nu(x)$, $Y_\nu(x)$, and their linear combinations with $\nu=0,1$. With Eq. (A2), we obtain

$$\frac{d}{dx}([Z_0(x) - iZ_1(x)]xe^{ix}) = \frac{d}{dx}([Z_0(x) + iZ_0'(x)]xe^{ix}) = Z_0(x)e^{ix}. \tag{A3}$$

Hence, the right-hand side can be integrated. We introduce the notations $u(x) \equiv J_0(x)e^{ix} = U'(x)$ and $v(x) \equiv Y_0(x)e^{ix} = V'(x)$, where

$$U(x) = [J_0(x) + iJ_0'(x)]xe^{ix}, \quad V(x) = [Y_0(x) + iY_0'(x)]xe^{ix}. \tag{A4}$$

Then, we consider the integral

$$K_{\alpha\beta} \equiv \int_a^b dx\alpha'(x)\beta(x), \tag{A5}$$

where α and β denote either U or V. It is obvious that

$$K_{\alpha\alpha} = \frac{1}{2}[\alpha(b)^2 - \alpha(a)^2]. \tag{A6}$$

Therefore, we obtain

$$K_{uu} = \frac{1}{2}[U(b)^2 - U(a)^2], \quad K_{vv} = \frac{1}{2}[V(b)^2 - V(a)^2]. \tag{A7}$$

The other components are manipulated as

$$K_{uv} = \int_a^b dxU'(x)V(x) = U(x)V(x)|_a^b - \int_a^b dxU(x)V'(x) = U(x)V(x)|_a^b - K_{vu}, \tag{A8}$$

which leads to

$$K_{uv} + K_{vu} = U(x)V(x)|_a^b. \tag{A9}$$

On the other hand, the difference is organized as

$$K_{uv} - K_{vu} = \int_a^b dxJ_0(x)e^{ix}xe^{ix}[Y_0(x) + iY_0'(x)] - (J \leftrightarrow Y) = i\int_a^b dx[J_0(x)Y_0'(x) - Y_0(x)J_0'(x)]xe^{2ix} = \frac{1}{\pi}(e^{2ib} - e^{2ia}), \tag{A10}$$

where we have used the Wronskian equation [Eq. (A1)]. Hence, we obtain

$$K_{uv} = \frac{1}{2\pi}(e^{2ib} - e^{2ia}) + \frac{1}{2}[U(b)V(b) - U(a)V(a)],$$

$$K_{vu} = \frac{-1}{2\pi}(e^{2ib} - e^{2ia}) + \frac{1}{2}[U(b)V(b) - U(a)V(a)]. \tag{A11}$$

By taking $a=v_c x/2$ and $b=v_s x/2$, the imaginary parts of $K_{\alpha\beta}$ gives the results for $I_{\alpha\beta}$ quoted in Eqs. (49)–(52).

[1] M. C. Gutzwiller, Phys. Rev. Lett. **10**, 159 (1963).
[2] W. F. Brinkman and T. M. Rice, Phys. Rev. B **2**, 1324 (1970).
[3] W. Metzner and D. Vollhardt, Phys. Rev. B **37**, 7382 (1988).
[4] Y. Kuramoto and H. Yokoyama, Phys. Rev. Lett. **67**, 1338 (1991).
[5] P. J. Forrester, Phys. Lett. A **196**, 353 (1995).
[6] M. Arikawa and Y. Saiga, J. Phys. A **39**, 10603 (2006).
[7] F. Gebhard and D. Vollhardt, Phys. Rev. B **38**, 6911 (1988).
[8] M. Kollar and D. Vollhardt, Phys. Rev. B **65**, 155121 (2002).
[9] M. Arikawa, T. Yamamoto, Y. Saiga, and Y. Kuramoto, Nucl. Phys. B **702**, 380 (2004).
[10] M. Arikawa, T. Yamamoto, Y. Saiga, and Y. Kuramoto, J. Phys. Soc. Jpn. **73**, 808 (2004).
[11] O. Narayan and Y. Kuramoto, Phys. Rev. B **73**, 195116 (2006).
[12] P. W. Anderson, B. S. Shastry, and D. Hristopulos, Phys. Rev. B **40**, 8939 (1989).
[13] This condition was stated wrongly in Paper I, and should be replaced by the present one.
[14] The minus sign for the cosine term in this expression and in Eq. (78) in Paper I was incorrectly written as a plus sign.
[15] Z. N. C. Ha and F. D. M. Haldane, Phys. Rev. Lett. **73**, 2887 (1994); **74**, 3501(E) (1995).
[16] Y. Kato and Y. Kuramoto, J. Phys. Soc. Jpn. **64**, 4518 (1995); unpublished.
[17] M. Arikawa (unpublished).
[18] M. Ogata and H. Shiba, Phys. Rev. B **41**, 2326 (1990).